Supplementary information to:

Mechanistic insights into the distinct functions of ATG16L1 in canonical autophagy and selective autophagy

Xinyu Gong, Yingli Wang, Yubin Tang, Jianping Liu, Ying Li, Yaru Wang, Xiaolong Xu, Mingfang Zhang, Miao Li, Yuchao Zhang, Liqiang Shen and Lifeng Pan*

Supplementary Figures

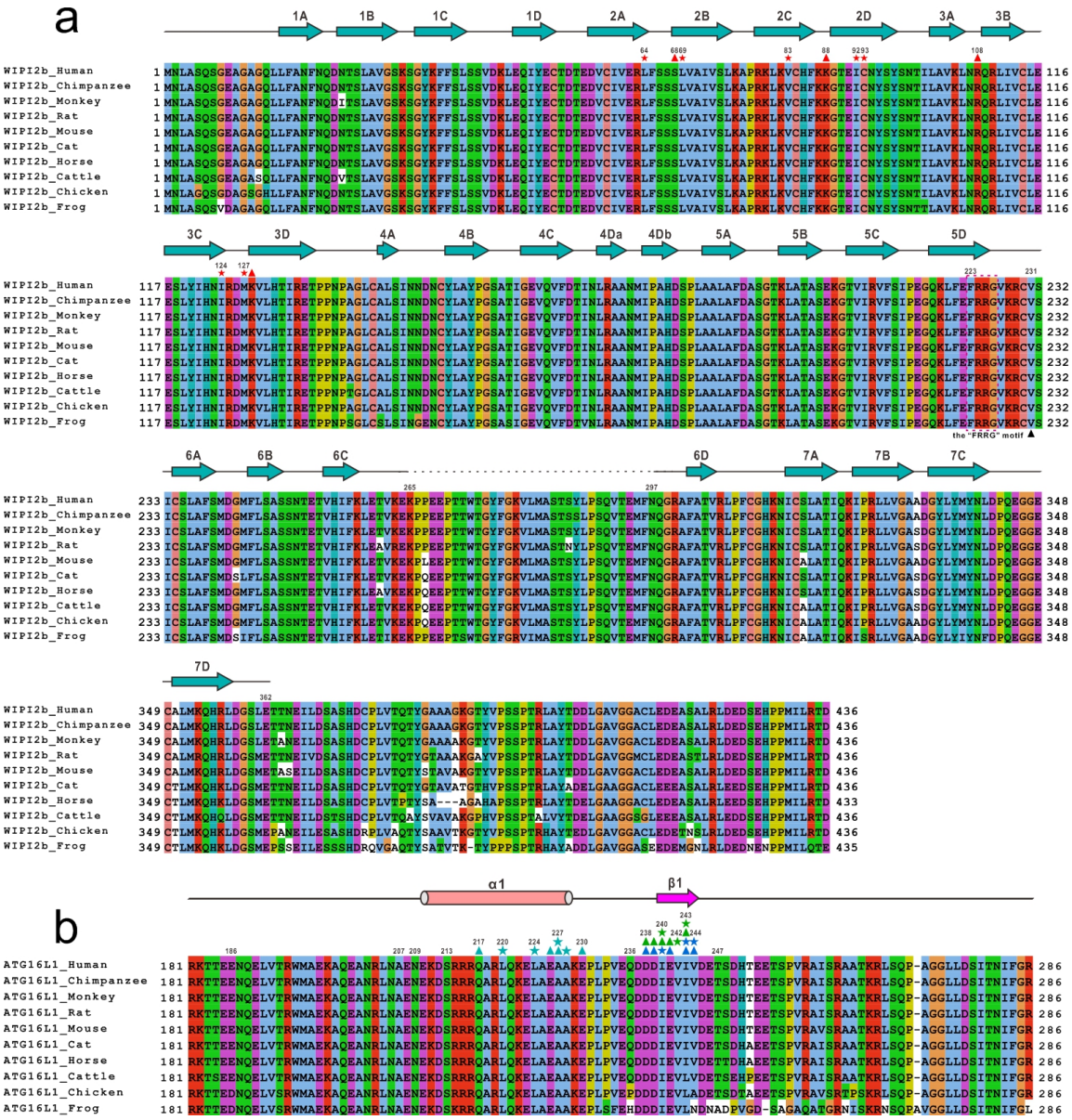

Supplementary Figure 1. Structure-based sequence alignment analyses of WIPI2b and ATG16L1. (**a**) Structure-based sequence alignment of WIPI2b from different species. The conserved residues are highlighted by colors using software Jalview 2.10.5 (http://www.jalview.org/). In this alignment, the conserved residues involved in hydrophobic interactions with ATG16L1 are highlighted with red stars while polar interactions with red triangles. The PI3P-binding "FRRG" motif is further boxed and highlighted. (**b**) Sequence alignment of ATG16L1(181-286) from different species. The conserved residues involved in hydrophobic interactions with WIPI2b are highlighted with cyan stars,

while polar interactions with cyan triangles. Meanwhile, the conserved residues of ATG16L1 involved in the interactions with RB1CC1 and GABARAPL1 are respectively highlighted with marine and green stars (hydrophobic interactions) or triangles (polar interactions).

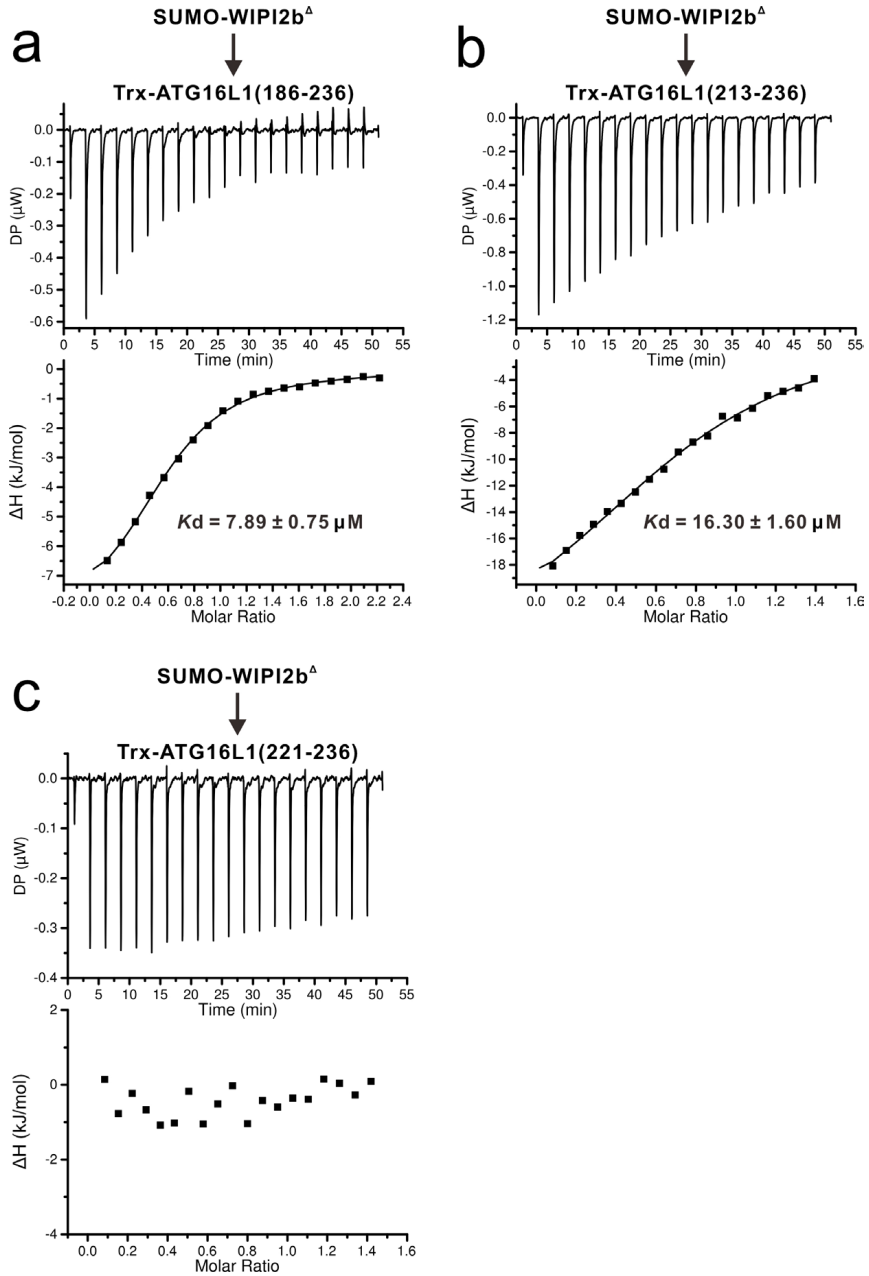

Supplementary Figure 2. Quantitative ITC-based mapping of the WIPI2b-binding region of ATG16L1. (a-c) ITC-based measurements of the binding affinities of SUMO-tagged WIPI2b with Trx-tagged ATG16L1(186-236) (**a**), ATG16L1(213-236) (**b**), and ATG16L1(221-236) (**c**). The *K*d

error is the fitted error obtained from the data analysis software, when using the one-site binding model to fit the ITC data. DP is the differential power measured by the ITC machine and ΔH is the enthalpy change measured by the ITC machine.

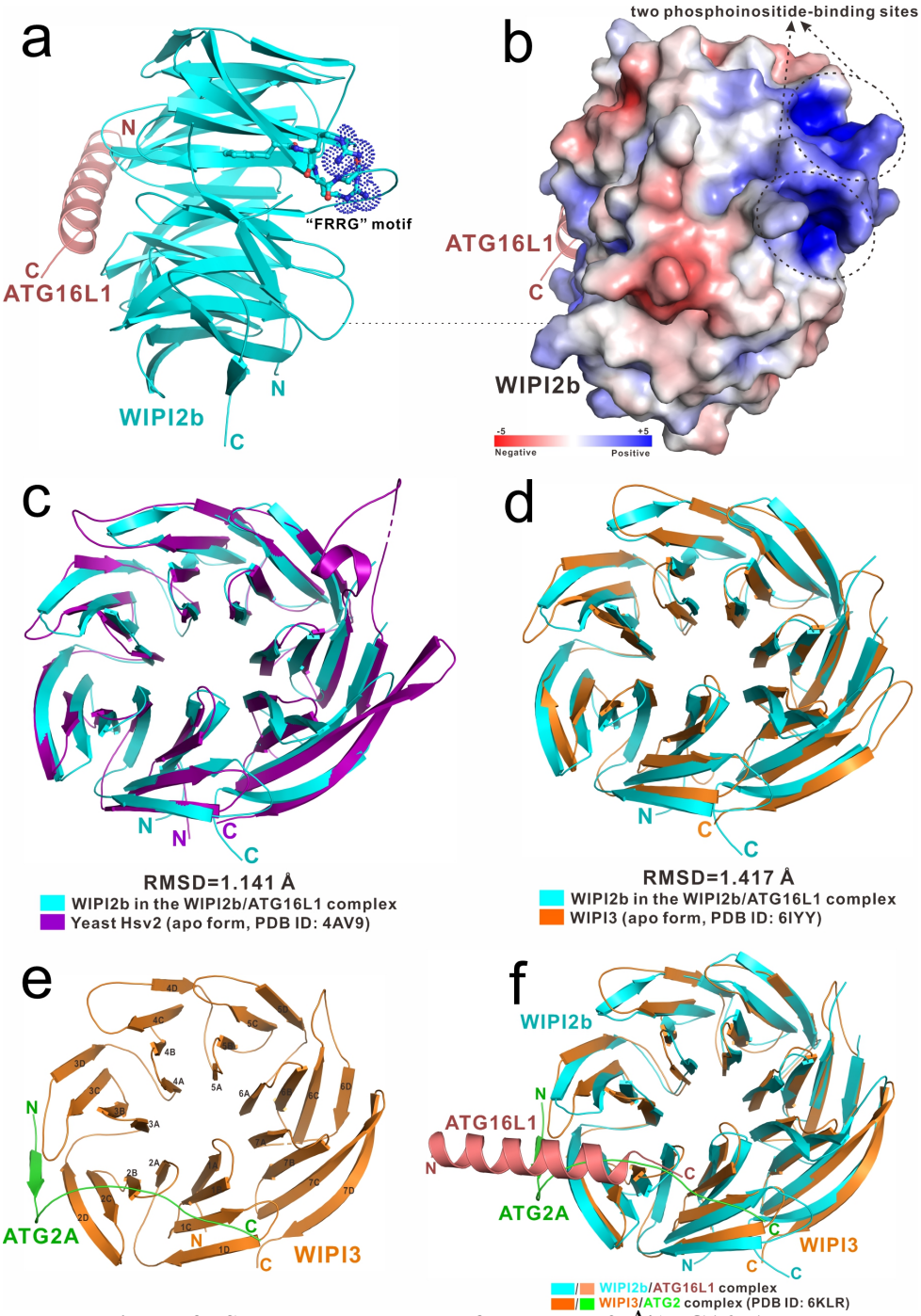

Supplementary Figure 3. Structural analyses of the WIPI2b$^{\Delta}$/ATG16L1 WBM complex. (a)

Ribbon-stick model showing the PI3P-binding "FRRG" motif of WIPI2b in the overall structure of the WIPI2b$^{\Delta}$/ATG16L1 WBM complex. In this drawing, the four residues in the "FRRG" motif of WIPI2b are highlighted in the stick-dot mode. (**b**) The combined surface charge representation and the ribbon model showing the two highly electropositive PI3P-binding sites of WIPI2b in the WIPI2b$^{\Delta}$/ATG16L1 WBM complex structure. (**c**) Ribbon diagram showing the structure comparison of WIPI2b in the WIPI2b$^{\Delta}$/ATG16L1 WBM complex with the yeast Hsv2 (PDB ID: 4AV9) that is colored in purple. (**d**) Ribbon diagram showing the structure comparison of WIPI2b in the WIPI2b$^{\Delta}$/ATG16L1 WBM complex with the apo-form WIPI3 (PDB ID: 6IYY) that is colored in orange. (**e**) The overall structure of WIPI3/ATG2A complex (PDB ID: 6KLR). In this drawing, WIPI3 is shown in orange and ATG2A in green. (**f**) The structure comparison of the WIPI2b/ATG16L1 complex and the WIPI3/ATG2A complex (PDB ID: 6KLR), which has the same orientation as that in panel **e**.

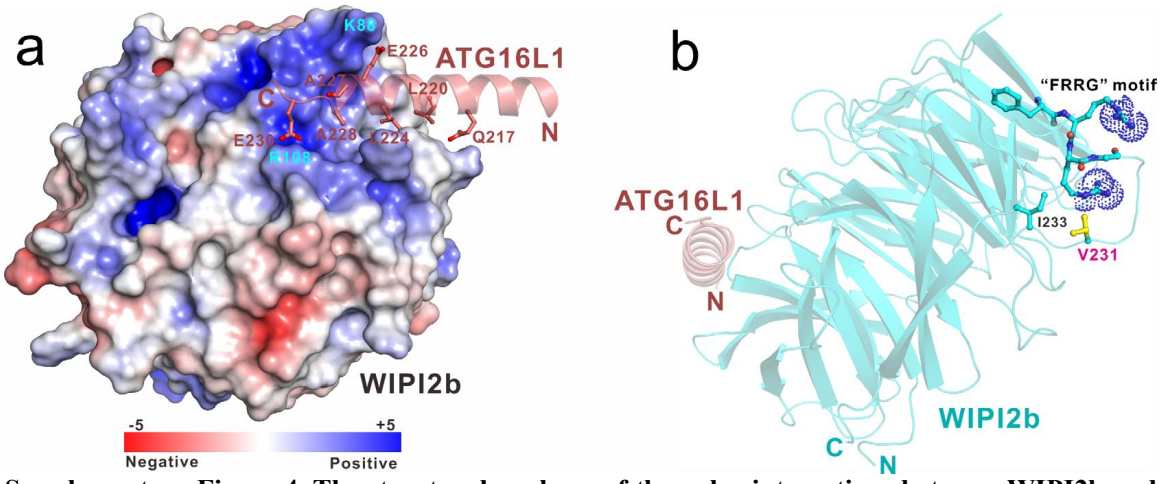

Supplementary Figure 4. The structural analyses of the polar interactions between WIPI2b and ATG16L1 WBM as well as the disease-associated V231M mutation of WIPI2b. (**a**) The combined surface charge representation and the ribbon-stick model showing the charge-charge interactions between WIPI2b$^{\Delta}$ and ATG16L1 WBM. (**b**) Ribbon-stick model showing the conformation as well as the structural arrangement of the disease-associated V231 residue in the WIPI2b/ATG16L1 complex structure. The side chain of V231 is highlighted in yellow.

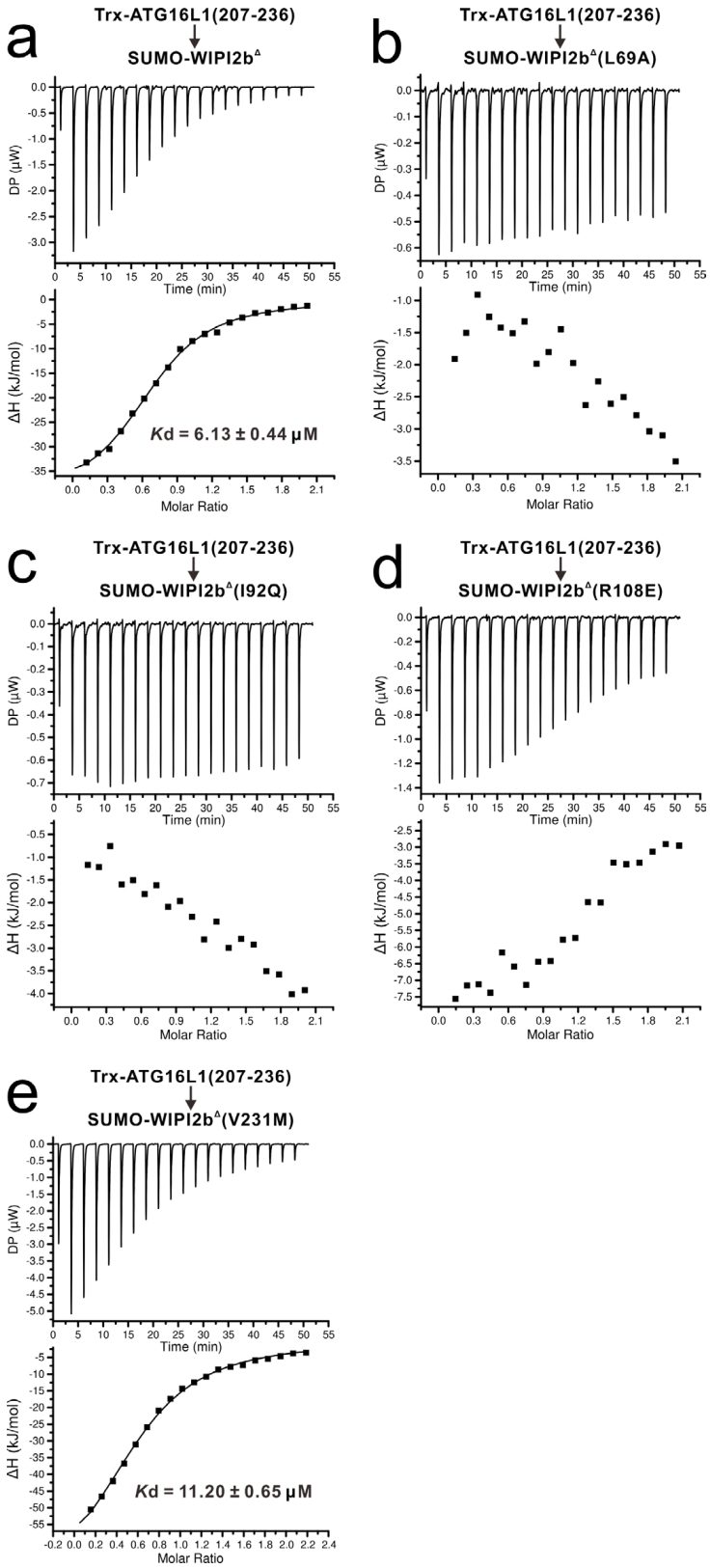

Supplementary Figure 5. ITC-based validations of the key WIPI2b interface residues observed in the WIPI2b$^{\Delta}$/ATG16L1 WBM complex structure. (**a-d**) ITC-based measurements of the binding

affinities of Trx-tagged ATG16L1 WBM with SUMO-tagged WIPI2b$^{\Delta}$ wild-type (**a**), L69A mutant (**b**), I92Q mutant (**c**), R108E mutant (**d**), and the disease-associated V231M mutant (**e**). *K*d values are the fitted dissociation constants with standard errors when using one-site binding model to fit the ITC data.

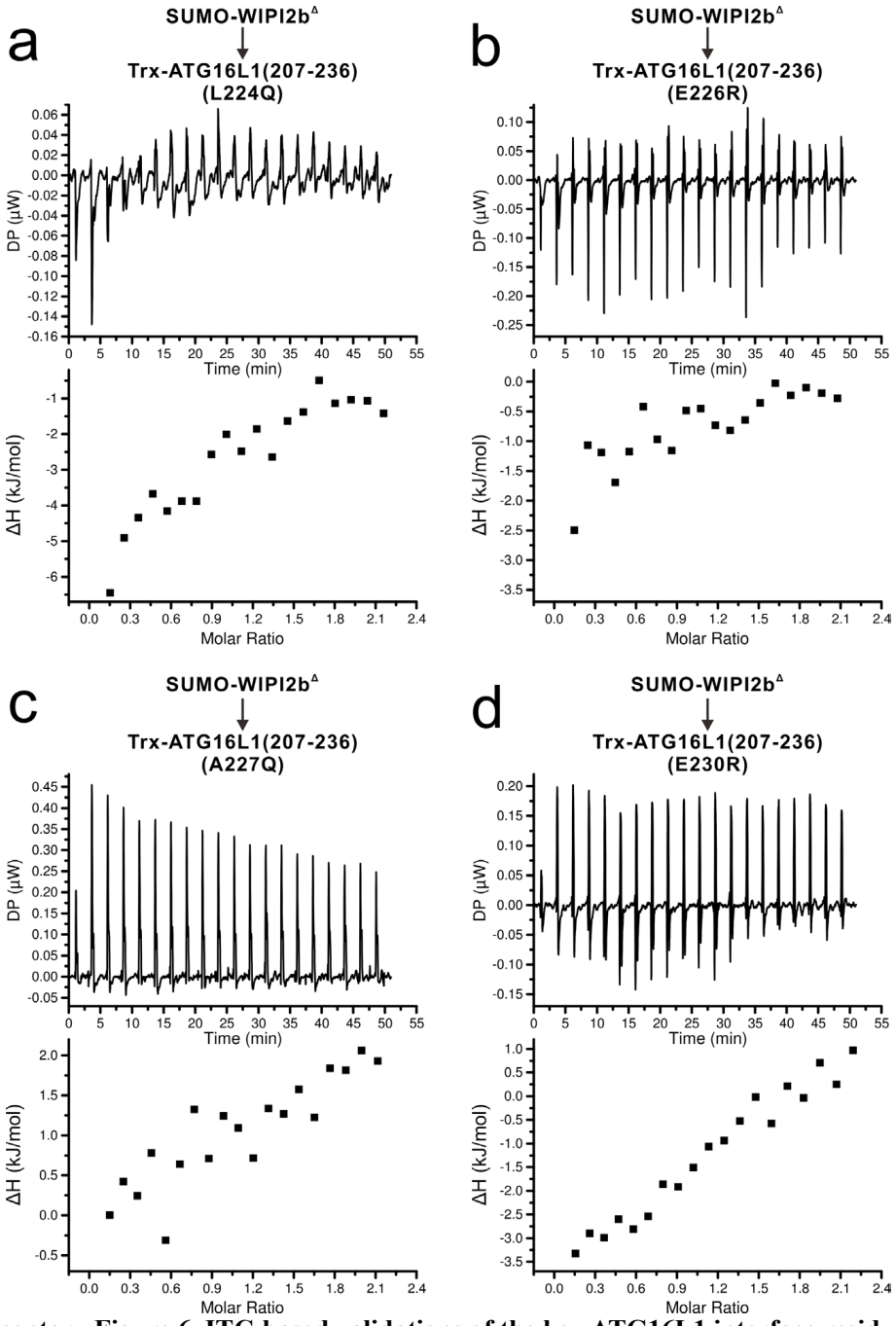

Supplementary Figure 6. ITC-based validations of the key ATG16L1 interface residues observed in the WIPI2b$^{\Delta}$/ATG16L1 WBM complex structure. (**a-d**) ITC-based measurements of the binding

affinities of SUMO-tagged WIPI2b$^{\Delta}$ with Trx-tagged ATG16L1 WBM L224Q mutant (**a**), E226R mutant (**b**), A227Q mutant (**c**), and E230R mutant (**d**). *K*d values are also the fitted dissociation constants with standard errors when using one-site binding model to fit the ITC data.

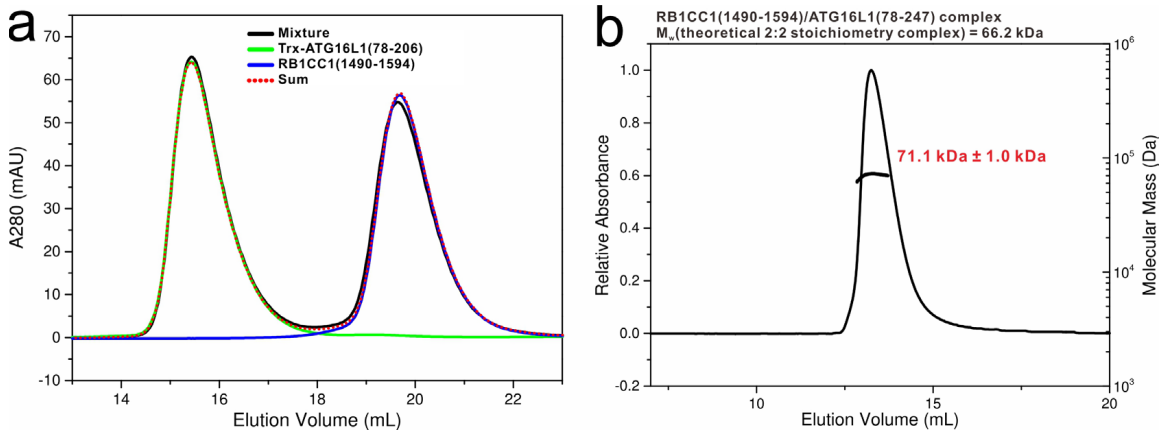

Supplementary Figure 7. Biochemical characterizations of the interaction between ATG16L1 and RB1CC1. (**a**) Analytical gel filtration chromatography analysis of the interaction of ATG16L1(78-206) with RB1CC1 Claw domain. (**b**) Multi-angle light-scattering analysis of the purified ATG16L1(78-247)/RB1CC1 Claw complex showing the relative light scattering signals as a function of elution volume. The derived molecular mass of the ATG16L1(78-247)/RB1CC1 Claw complex is shown in red. The molecular mass error is the fitted error obtained from the data analysis software.

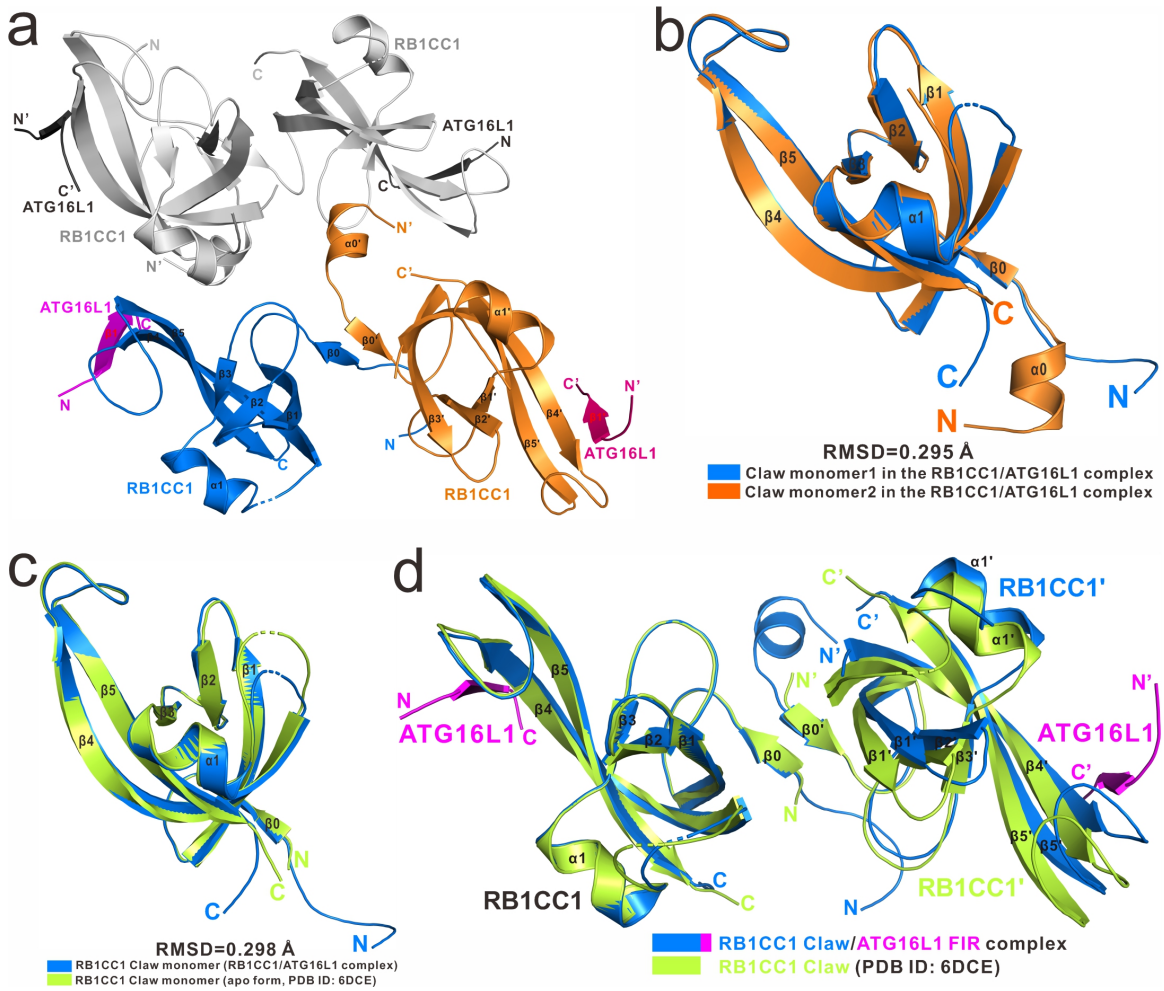

Supplementary Figure 8. The structural analyses of the RB1CC1 Claw/ATG16L1 FIR complex. (**a**) Ribbon diagram showing that an adjacent RB1CC1 Claw/ATG16L1 FIR complex (grey) directly packs against the N-terminal α0-helix of one monomeric RB1CC1 Claw (orange) in the crystal packing. Thus, the unique N-terminal α0-helix of one monomeric RB1CC1 Claw in the RB1CC1 Claw/ATG16L1 FIR complex structure is induced by the effect of crystal packing. (**b**) The structural comparison of the two monomeric RB1CC1 Claw domains in the RB1CC1 Claw/ATG16L1 FIR complex. (**c**) The comparison of the overall structures of the representative monomeric RB1CC1 Claw domain in the apo form (green, PDB ID: 6DCE) and in the RB1CC1 Claw/ATG16L1 FIR complex (blue). (**d**) Ribbon representation showing the structural comparison of apo-form RB1CC1 Claw dimer (green, PDB ID: 6DCE) with the RB1CC1 Claw/ATG16L1 FIR complex (blue/magenta). In this drawing, the two dimeric structures are overlaid by aligning selected one RB1CC1 Claw monomer in these two structures.

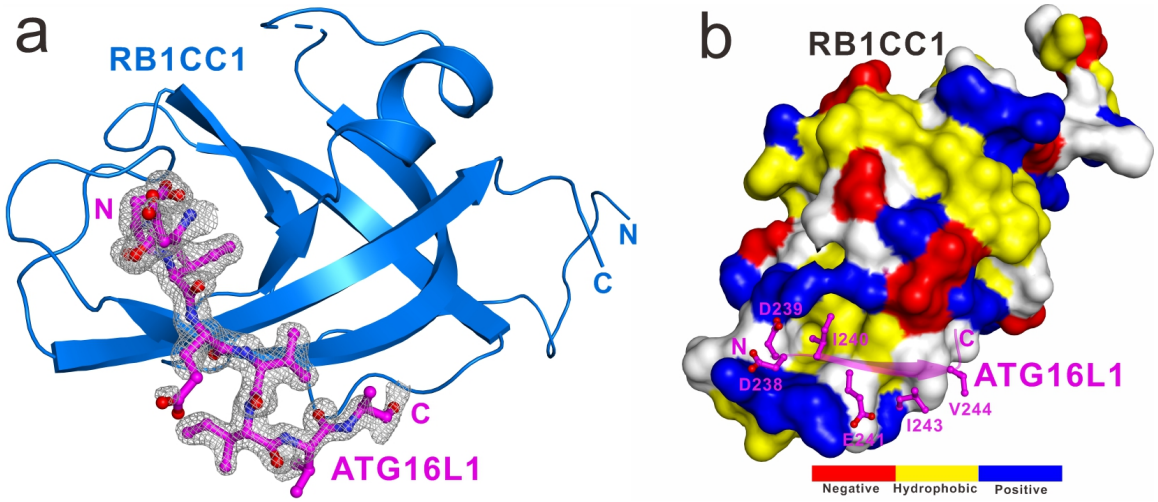

Supplementary Figure 9. Structural analyses of the detailed interaction between RB1CC1 Claw and ATG16L1 FIR. (**a**) The 2mFo-DFc map of the bound ATG16L1 FIR in the RB1CC1 Claw/ ATG16L1 FIR complex structure. The electron density map is calculated by omitting the ATG16L1 FIR peptide from the final PDB file and contoured at 1.6σ. (**b**) The combined surface representation and the ribbon-stick model showing the hydrophobic binding surface between RB1CC1 Claw and ATG16L1 FIR. In this drawing, the ATG16L1 FIR is displayed in the ribbon-stick model, and the RB1CC1 is showed in surface representation. Particularly, the hydrophobic amino acid residues in the surface model of RB1CC1 Claw are drawn in yellow, the positively charged residues in blue, the negatively charged residues in red, and the uncharged polar residues in gray.

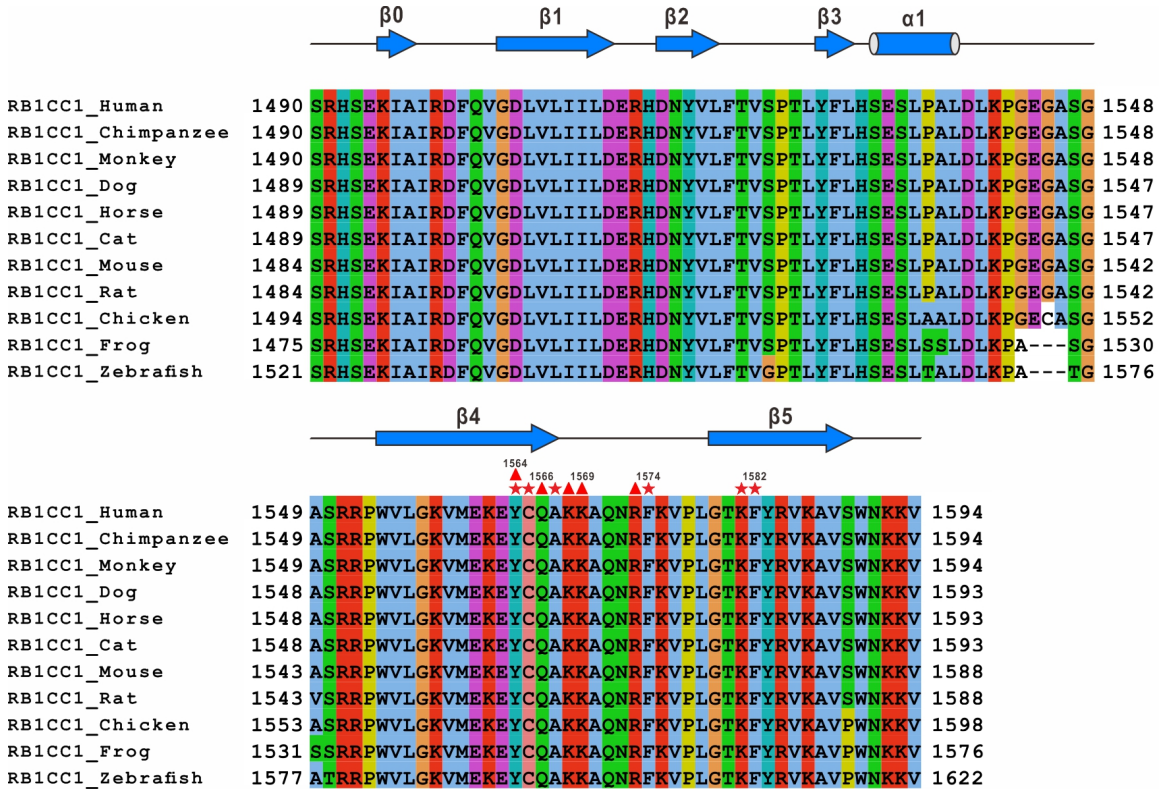

Supplementary Figure 10. Structure-based sequence alignment analysis of RB1CC1 Claw. The conserved residues are highlighted by colors using software Jalview 2.10.5 (http://www.jalview.org/). In this alignment, the conserved residues of RB1CC1 Claw involved in the binding with ATG16L1 FIR are labeled with red stars (hydrophobic interactions) or red triangles (polar interactions).

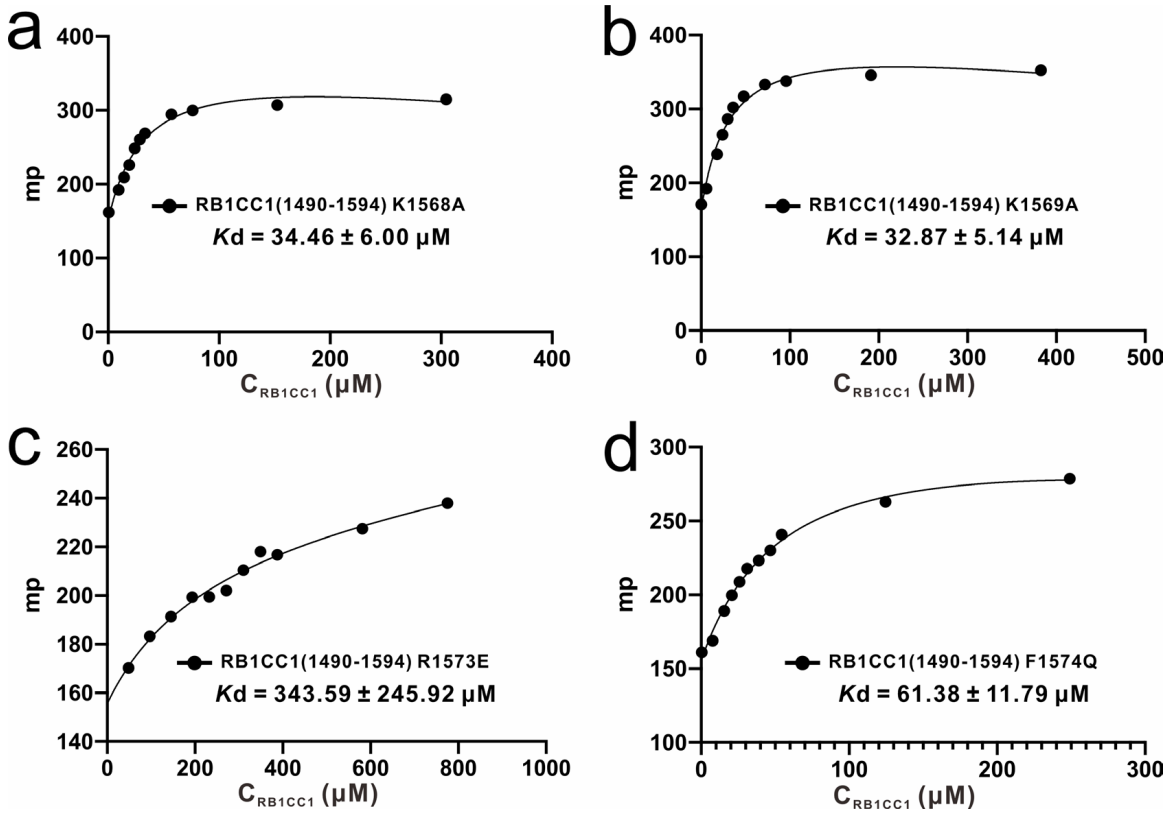

Supplementary Figure 11. Quantitative FP-based validations of the key interface residues of RB1CC1 in the RB1CC1 Claw/ATG16L1 FIR complex structure. (**a-d**) FP assay reveals the binding affinities of FITC-labeled ATG16L1 FIR with the RB1CC1 Claw K1568A mutant (**a**), K1569A mutant (**b**), R1573E mutant (**c**), and F1574Q mutant (**d**). *K*d values are the fitted dissociation constants with standard errors, when using the one-site binding model to fit the FP data.

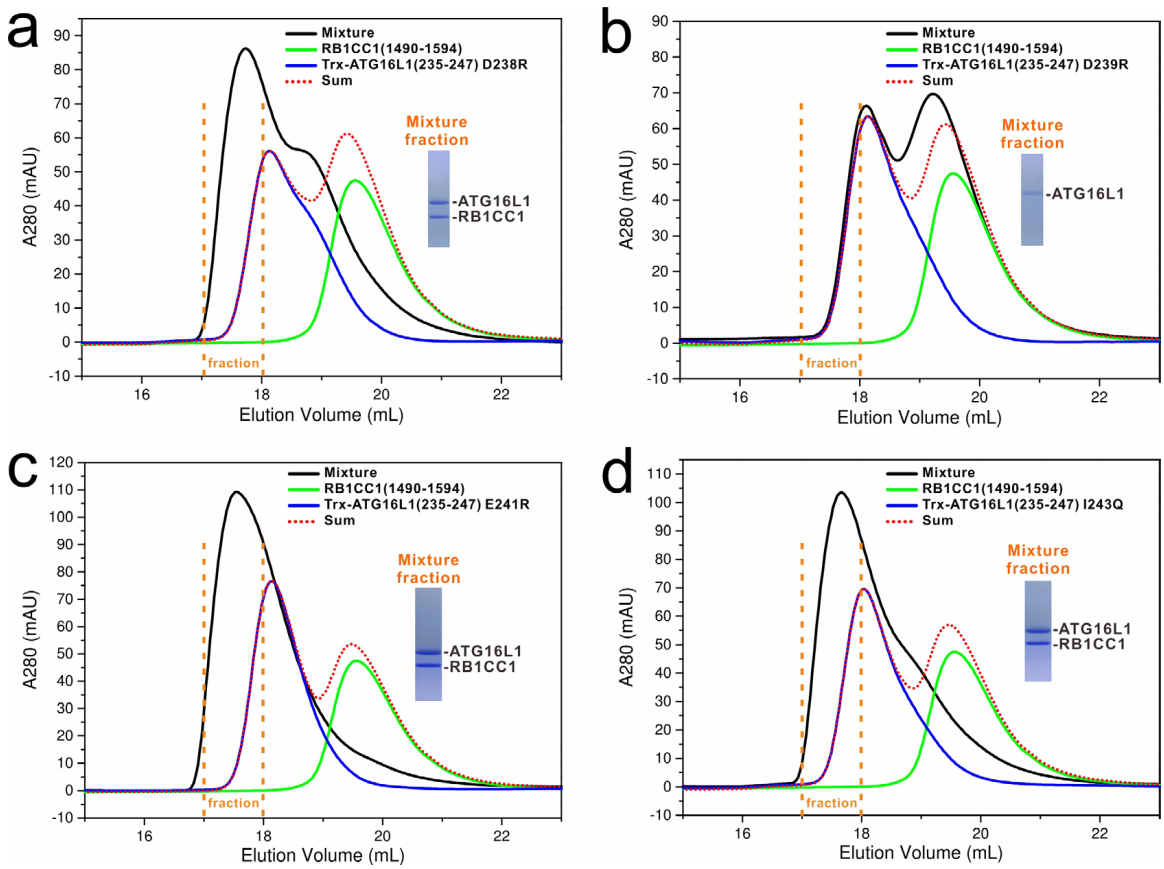

Supplementary Figure 12. Analytic gel filtration chromatography analyses-based validations of the key interface residues of ATG16L1 FIR in the RB1CC1 Claw/ATG16L1 FIR complex structure. (**a-d**) Analytic gel filtration chromatography-based analyses of the interactions of RB1CC1 Claw domain with ATG16L1 FIR D238R mutant (**a**), D239R mutant (**b**), E241R mutant (**c**), and I243Q mutant (**d**). The insert in each panel shows the SDS-PAGE combined with Coomassie blue staining analysis of the protein components of the indicated "Mixture fraction" fraction collected from the analytical gel filtration chromatography experiment of the "Mixture" sample (the black curve).

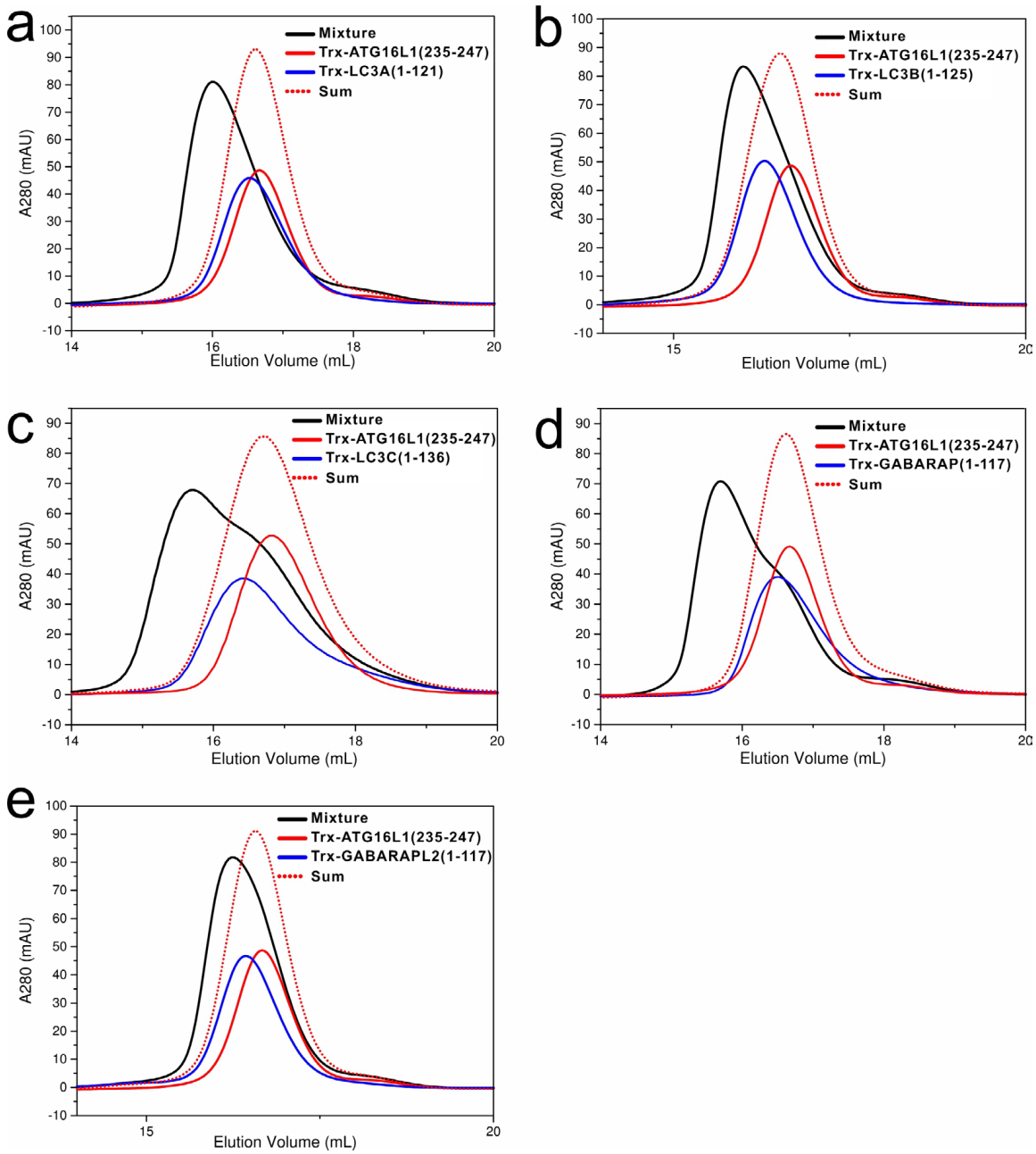

Supplementary Figure 13. Biochemical characterizations of the interactions between ATG16L1 FIR and five mammalian ATG8 family proteins. (**a-d**) Analytic gel filtration chromatography-based analysis of the interaction of ATG16L1 FIR with LC3A (**a**), LC3B (**b**), LC3C (**c**), GABARAP (**d**) and GABARAPL2 (**e**). These results indicate that ATG16L1 FIR can directly interact with mammalian ATG8 family proteins.

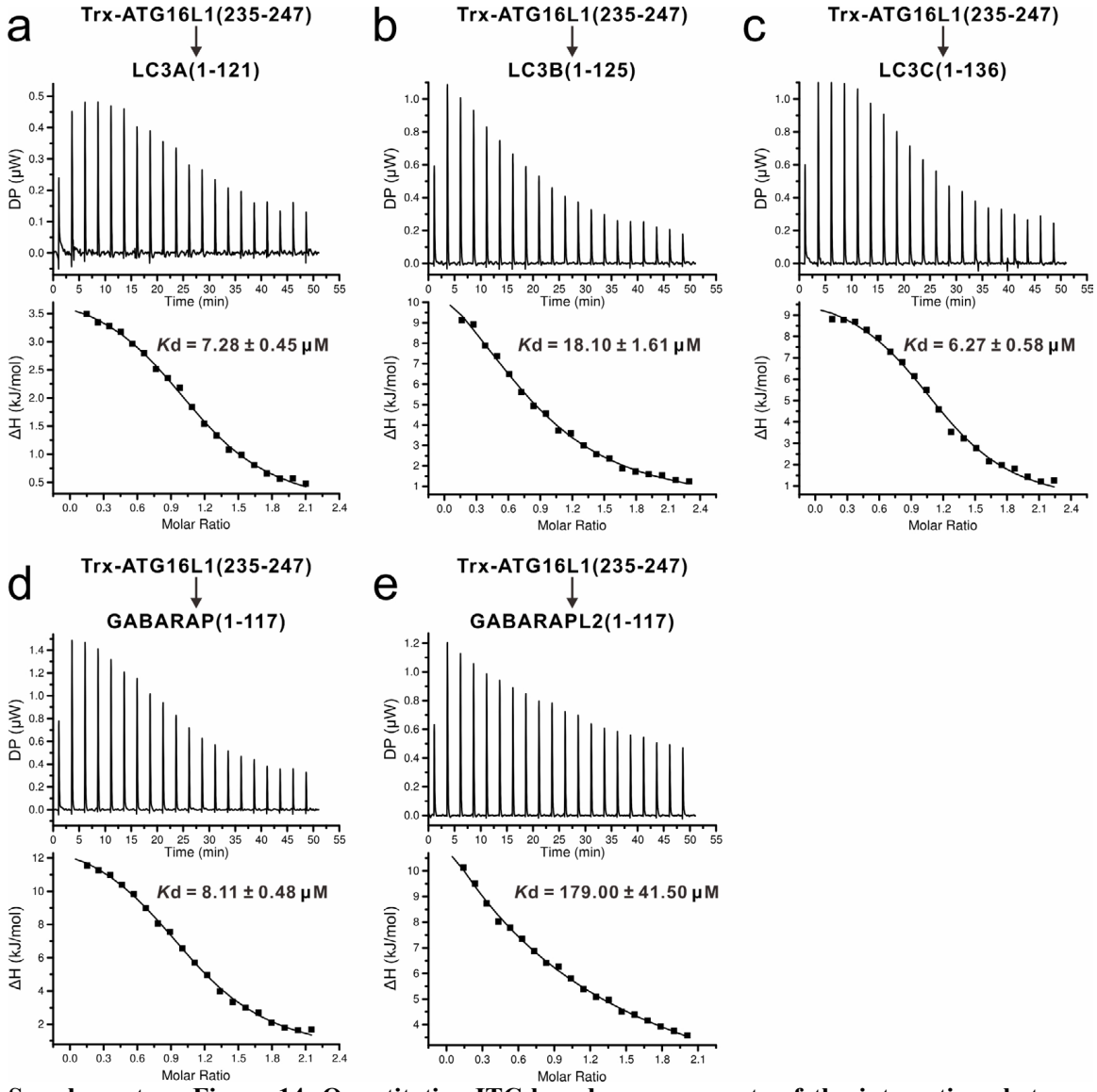

Supplementary Figure 14. Quantitative ITC-based measurements of the interactions between ATG16L1 FIR and five mammalian ATG8 family proteins. (**a-e**) ITC-based measurements of the binding affinities of ATG16L1 FIR with LC3A (**a**), LC3B (**b**), LC3C (**c**), GABARAP (**d**) and GABARAPL2 (**e**). *K*d values are the fitted dissociation constants with standard errors when using one-site binding model to fit the ITC data.

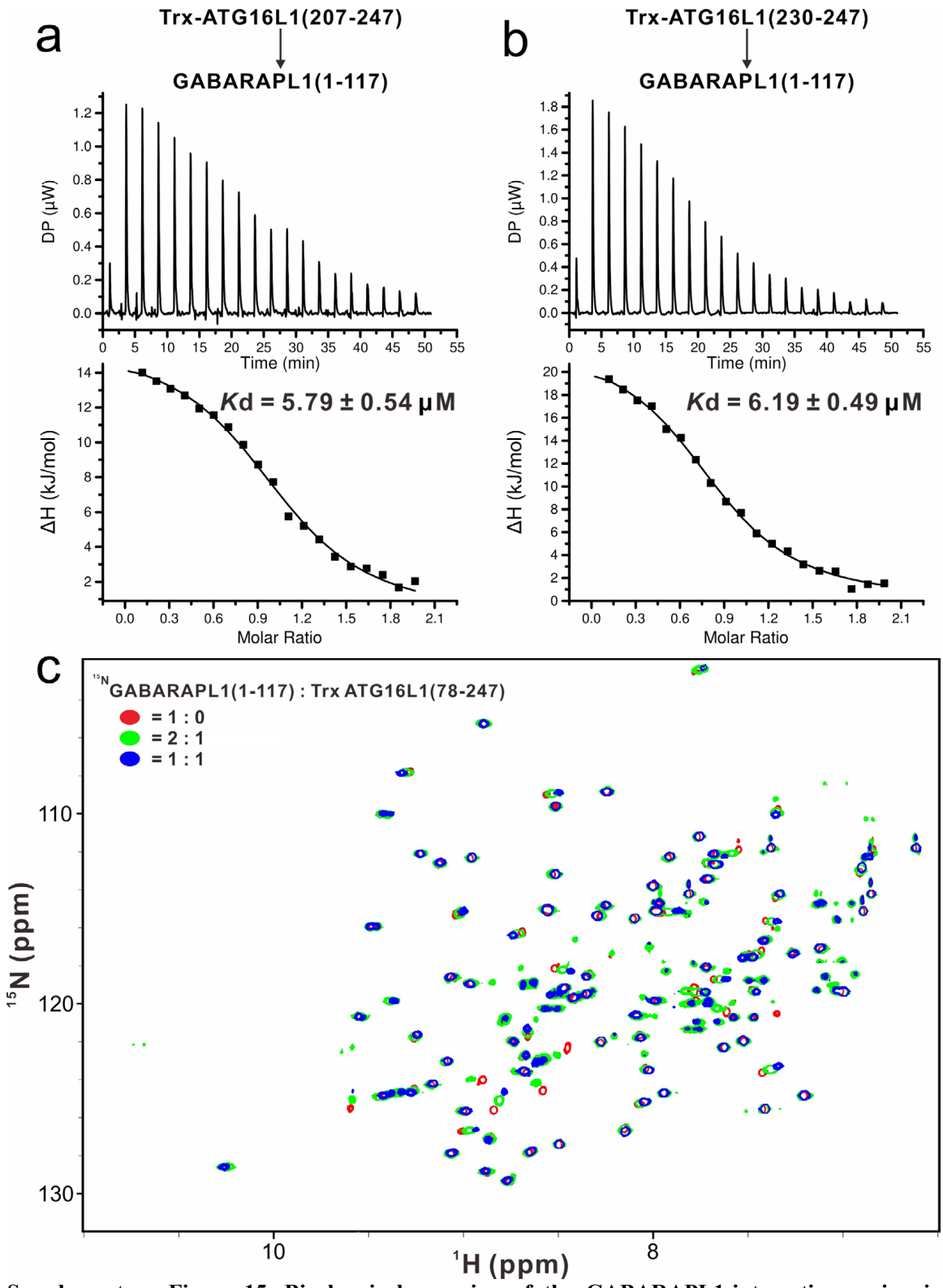

Supplementary Figure 15. Biochemical mapping of the GABARAPL1-interacting region in ATG16L1. (**a** and **b**) ITC-based measurements of the binding affinities of GABARAPL1 with Trx-tagged ATG16L1(207-247) (**a**) and ATG16L1(230-247) (**b**). *K*d values are the fitted dissociation

constants with standard errors when using one-site binding model to fit the ITC data. (**c**) Superposition plots of the ^{1}H-^{15}N HSQC spectra of GABARAPL1 titrated with the un-labeled Trx-tagged ATG16L1(78-247) at different molar ratios.

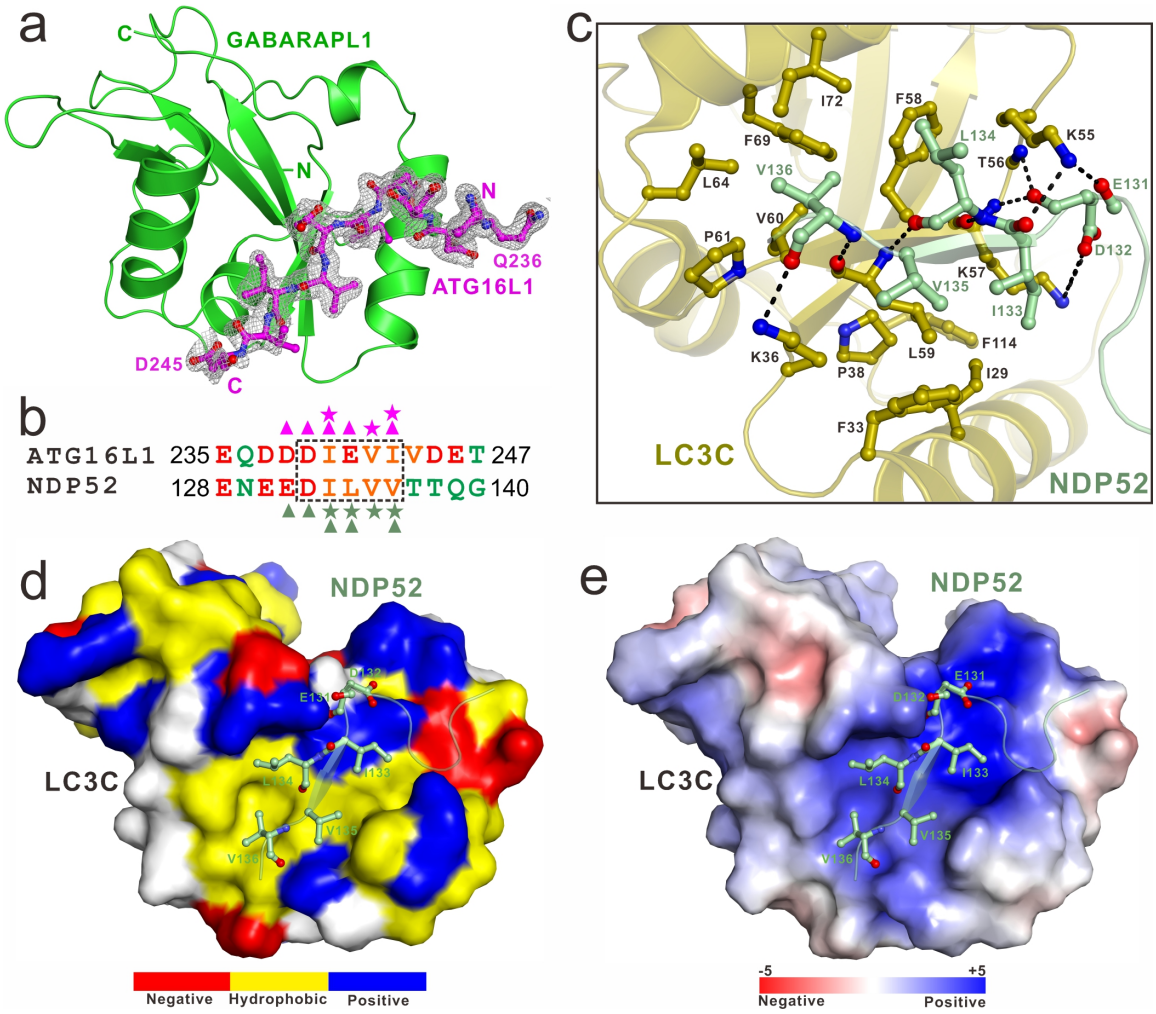

Supplementary Figure 16. The comparison of GABARAPL1/ATG16L1 FIR complex with the NDP52 LIR/LC3C complex. (**a**) The 2mFo-DFc map of the bound ATG16L1 FIR in the GABARAPL1/ATG16L1 FIR complex structure. The electron density map is calculated by omitting the ATG16L1 FIR peptide from the final PDB file and contoured at 1.6σ. (**b**) Sequence alignment analysis of ATG16L1 FIR and NDP52 LIR. The residues of ATG16L1 involved in hydrophobic interactions with GABARAPL1 are highlighted with magenta stars while polar interactions with magenta triangles. The residues of NDP52 involved in interactions with LC3C are highlighted by pale

green stars (hydrophobic interaction) or triangles (polar interaction). (**c**) Ribbon-stick model showing the detailed interactions between NDP52 and LC3C in the NDP52 LIR/LC3C complex structure (PDB ID: 3VVW). The hydrogen bonds and salt bridges involved in the binding are shown as dotted lines. (**d**) The combined surface representation and the ribbon-stick model showing the hydrophobic binding surface between NDP52 and LC3C in the NDP52 LIR/LC3C complex structure. In this drawing, NDP52 LIR is displayed in the ribbon-stick model, and LC3C is showed in surface representation colored by amino acid types. Specifically, the hydrophobic residues in the surface model of LC3C are drawn in yellow, the positively charged residues in blue, the negatively charged residues in red, and the uncharged polar residues in gray. (**e**) The combined surface charge representation and the ribbon-stick model showing the charge-charge interactions between NDP52 LIR and LC3C.

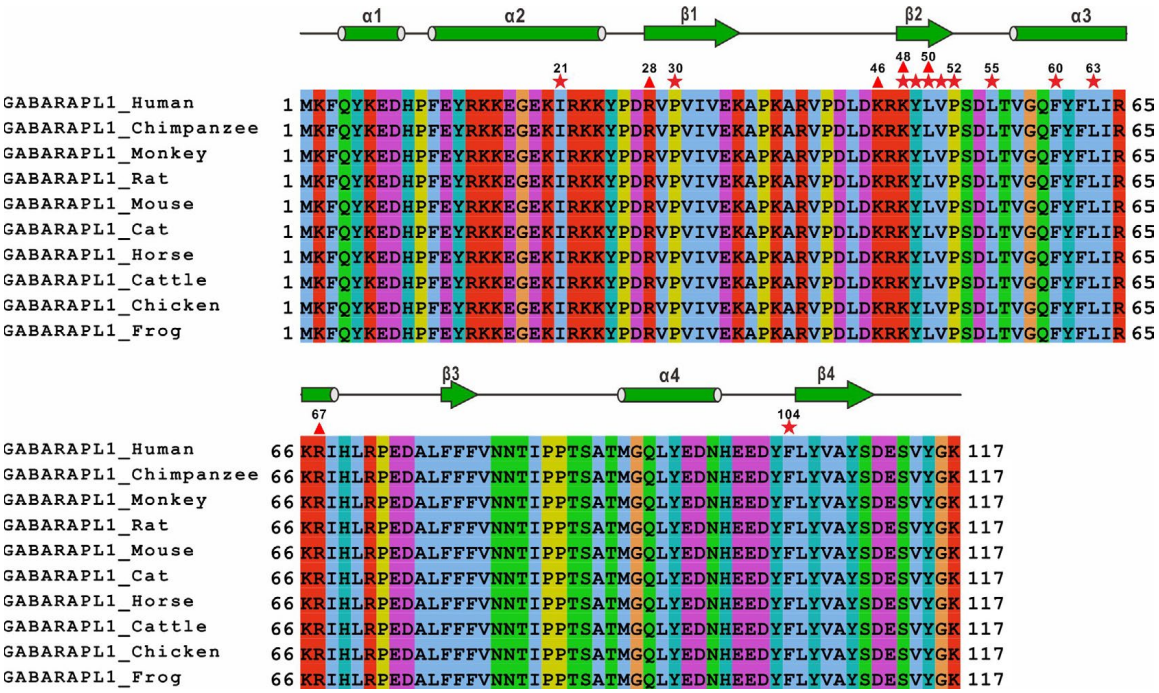

Supplementary Figure 17. Structure-based sequence alignment analysis of GABARAPL1. Structure-based sequence alignment of GABARAPL1 from different species. In this alignment, the conserved residues are highlighted by colors using software Jalview 2.10.5 (http://www.jalview.org/), and the residues of GABARAPL1 involved in the binding with ATG16L1 FIR are labeled with red stars (hydrophobic interactions) or red triangles (polar interactions).

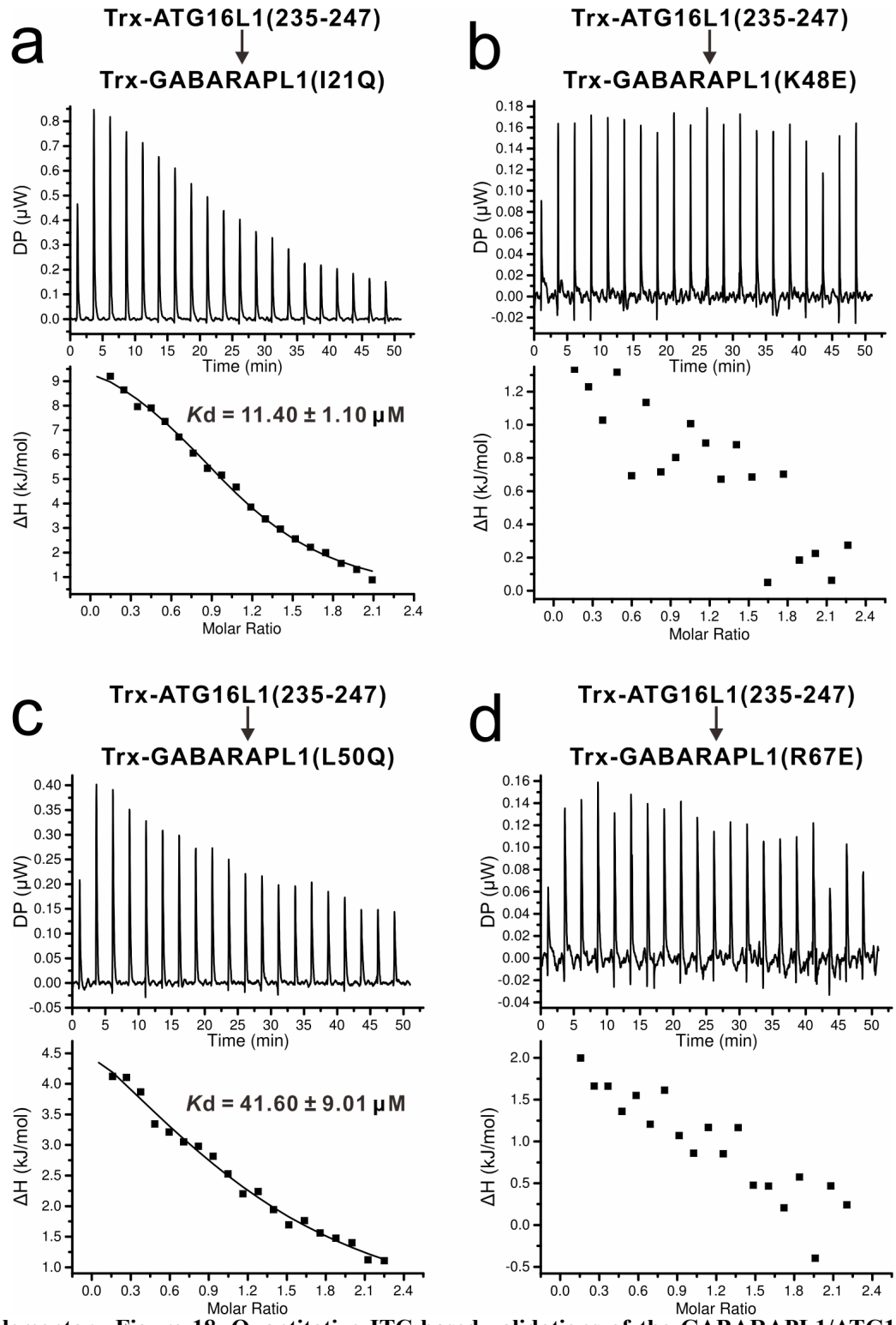

Supplementary Figure 18. Quantitative ITC-based validations of the GABARAPL1/ATG16L1 FIR complex structure by mutations of key interface residues of GABARAPL1. (**a-e**) ITC-based measurements of the binding affinities of Trx-tagged ATG16L1 FIR with Trx-tagged GABARAPL1

I21Q mutant (**a**), K48E mutant (**b**), L50Q mutant (**c**), and R67E mutant (**d**). *K*d values are the fitted dissociation constants with standard errors when using one-site binding model to fit the ITC data.

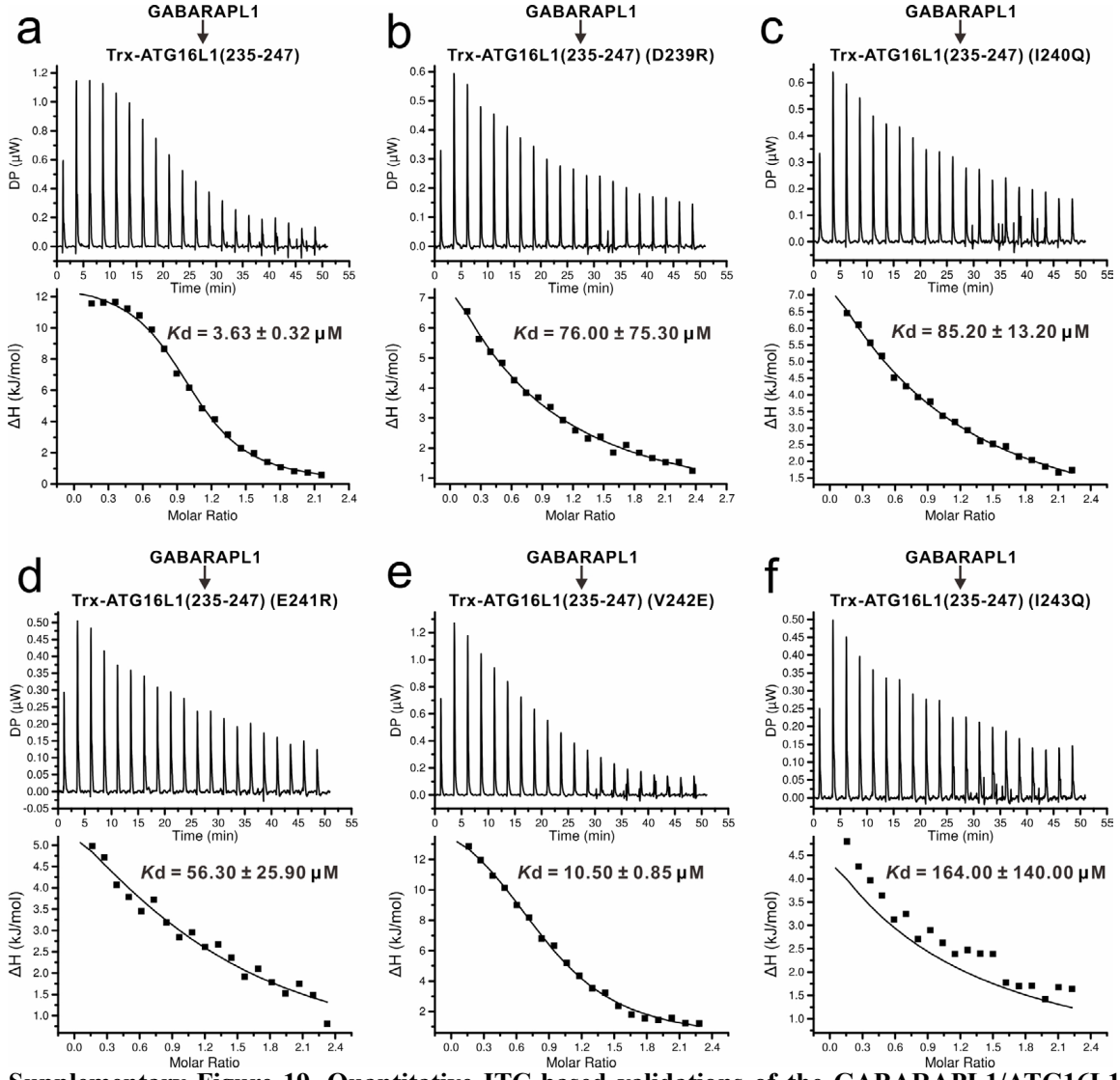

Supplementary Figure 19. Quantitative ITC-based validations of the GABARAPL1/ATG16L1 FIR complex structure by mutations of key interface residues of ATG16L1 FIR. (**a-f**) ITC-based measurements of the binding affinities of GABARAPL1 with Trx-tagged ATG16L1 FIR wild-type (**a**), D239R mutant (**b**), I240Q mutant (**c**), E241R mutant (**d**), V242E mutant (**e**), and I243Q mutant (**f**). *K*d values are the fitted dissociation constants with standard errors when using one-site binding model to fit the ITC data.

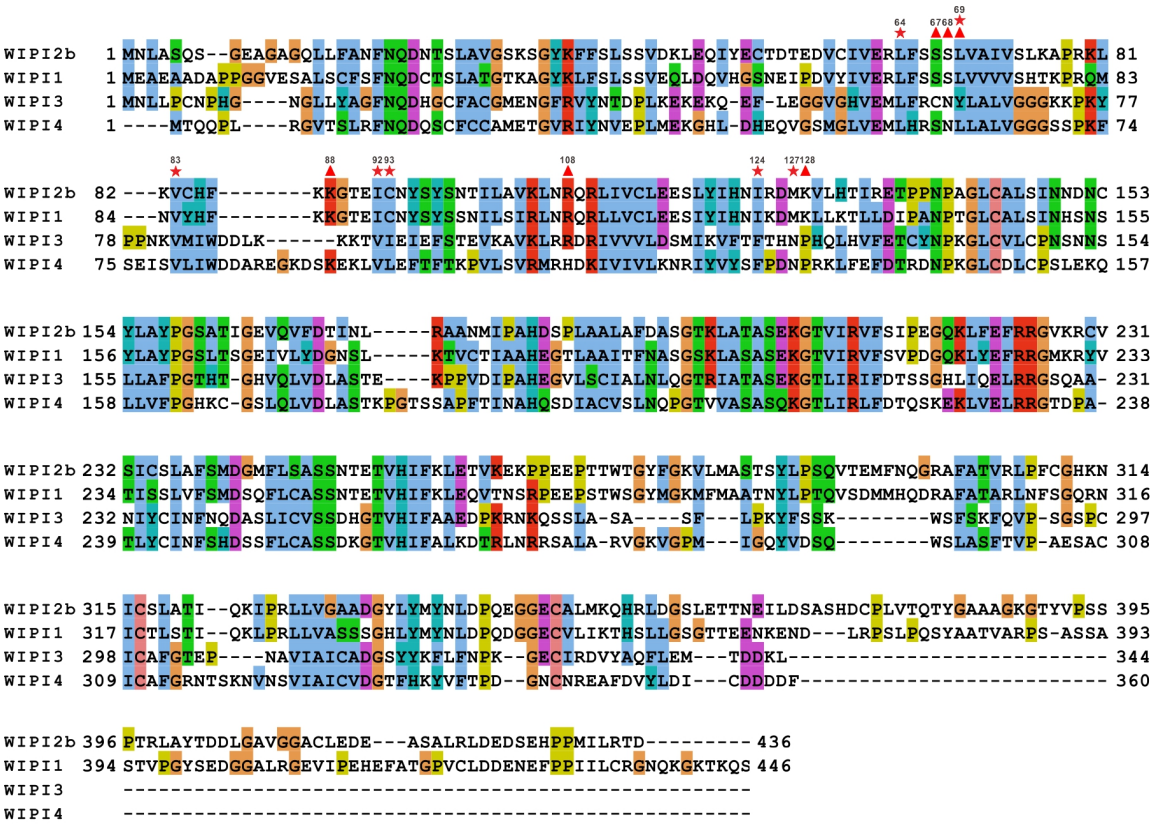

Supplementary Figure 20. Sequence alignment analysis of four WIPI proteins from human species. The conserved residues are highlighted by colors using software Jalview 2.10.5 (http://www.jalview.org/). In this alignment, the residues of WIPI2b that are involved in the binding with ATG16L1 WBM are labeled with red triangles (polar interactions) or red stars (hydrophobic interactions).

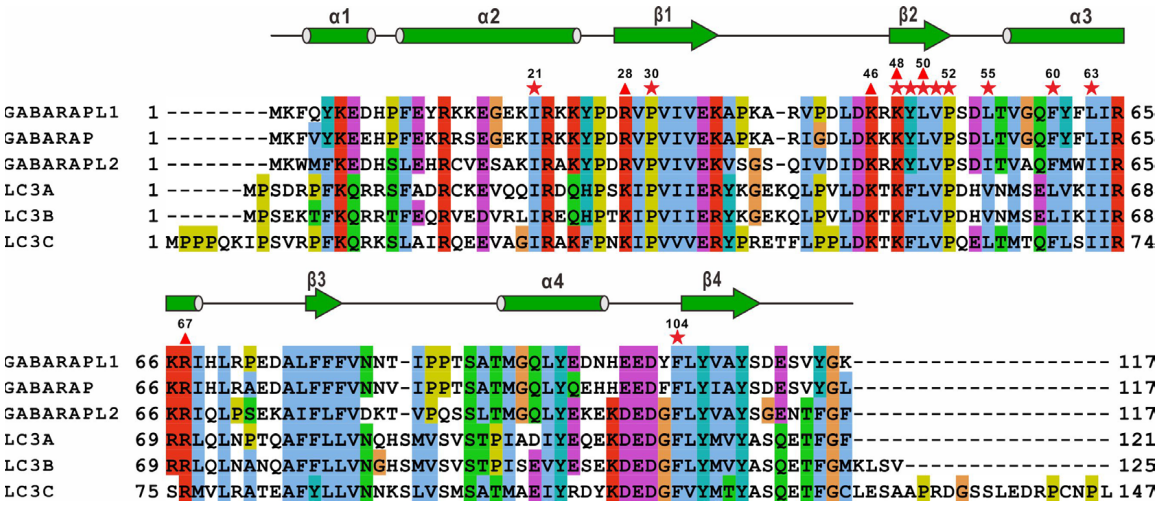

Supplementary Figure 21. Structure-based sequence alignment of six ATG8 family proteins from human species. In this alignment, the residues of GABARAPL1 that are involved in the binding with ATG16L1 FIR are labeled with red triangles (polar interactions) or red stars (hydrophobic interactions). The conserved residues are highlighted by colors using software Jalview 2.10.5 (http://www.jalview.org/).

Supplementary Table 1. Statistics of X-ray crystallographic data collection and model refinement of the WIPI2b/ATG16L1(207-236) complex

Data set	WIPI2b/ATG16L1(207-236) complex
Data collection	
Space group	$P6_3$
Unit cell parameters	
a, b, c (Å)	97.944, 97.944, 65.581
α, β, γ (°)	90, 90, 120
Wavelength (Å)	0.97917
Resolution range (Å)	100.00-1.50 (1.53-1.50)
Number of total reflections	114418 (11463)
Number of unique reflections	57223 (5263)
Redundancy	2.0 (2.0)
$I/\sigma I$	9.06 (3.77)
Completeness (%)	98.41 (91.79)
R_{merge} (%) [a]	6.13 (16.36)
Structure refinement	
Resolution (Å)	28.80-1.50 (1.55-1.50)
R_{work} [b]/R_{free} [c] (%)	18.20 (23.11) / 19.67 (27.36)
Number of reflections	
working set	56356 (5263)
test set	2884 (244)
B factor (Å^2)	
average	20.28
protein	12.64
RMSD bonds (Å)	0.012
RMSD angles (°)	1.15
Number of non-hydrogen atoms	
protein	2635
ligand	0
water	201
Ramachandran plot (%)	
most favored	99.09
additionally allowed	0.91
outliers	0.00

[a] $R_{merge} = \sum|I_i - I_m|/\sum I_i$, where I_i is the intensity of the measured reflection and I_m is the mean intensity of all symmetry related reflections.

[b] $R_{work} = \Sigma||F_{obs}| - |F_{calc}||/\Sigma|F_{obs}|$, where F_{obs} and F_{calc} are observed and calculated structure factors.

[c] $R_{free} = \Sigma_T||F_{obs}| - |F_{calc}||/\Sigma_T|F_{obs}|$, where T is a test data set of about 5% of the total reflections randomly chosen and set aside prior to refinement.

Numbers in parentheses represent the value for the highest resolution shell.

Supplementary Table 2. Statistics of X-ray crystallographic data collection and model refinement of the RB1CC1 Claw/ATG16L1 FIR complex

Data set	RB1CC1 Claw/ATG16L1 FIR complex
Data collection	
Space group	$P12_11$
Unit cell parameters	
a, b, c (Å)	58.701, 34.894, 60.727
α, β, γ (°)	90, 118.377, 90
Wavelength (Å)	0.97918
Resolution range (Å)	53.43-1.61 (1.64-1.61)
Number of total reflections	55485 (5477)
Number of unique reflections	27848 (2788)
Redundancy	2.0 (2.0)
$I/\sigma I$	17.69 (2.66)
Completeness (%)	97.83 (98.55)
R_{merge} (%) [a]	1.53 (23.08)
Structure refinement	
Resolution (Å)	22.46-1.61 (1.67-1.61)
R_{work} [b]/R_{free} [c] (%)	17.80 (26.13) / 21.57 (29.08)
Number of reflections	
working set	27801 (2784)
test set	1303 (120)
B factor (Å^2)	
average	40.91
protein	25.26
RMSD bonds (Å)	0.014
RMSD angles (°)	1.27
Number of non-hydrogen atoms	
protein	1713
ligand	0
water	139
Ramachandran plot (%)	
most favored	98.48
additionally allowed	1.52
outliers	0.00

[a] $R_{merge} = \sum|I_i - I_m|/\sum I_i$, where I_i is the intensity of the measured reflection and I_m is the mean intensity of all symmetry related reflections.

[b] $R_{work} = \Sigma||F_{obs}| - |F_{calc}||/\Sigma|F_{obs}|$, where F_{obs} and F_{calc} are observed and calculated structure factors.

[c] $R_{free} = \Sigma_T||F_{obs}| - |F_{calc}||/\Sigma_T|F_{obs}|$, where T is a test data set of about 5% of the total reflections randomly chosen and set aside prior to refinement.

Numbers in parentheses represent the value for the highest resolution shell.

Supplementary Table 3. Statistics of X-ray crystallographic data collection and model refinement of the GABARAPL1/ATG16L1 FIR complex

Data set	GABARAPL1/ATG16L1 FIR complex
Data collection	
Space group	$P22_12_1$
Unit cell parameters	
a, b, c (Å)	38.141, 65.429, 109.795
α, β, γ (°)	90, 90, 90
Wavelength (Å)	0.97918
Resolution range (Å)	56.21-1.54 (1.57-1.54)
Number of total reflections	81232 (8200)
Number of unique reflections	40633 (4100)
Redundancy	2.0 (2.0)
$I/\sigma I$	12.51 (2.63)
Completeness (%)	97.68 (99.49)
R_{merge} (%) [a]	1.38 (15.99)
Structure refinement	
Resolution (Å)	21.39-1.54 (1.60-1.54)
R_{work} [b]/R_{free} [c] (%)	18.94 (27.07) / 22.14 (27.20)
Number of reflections	
working set	40523 (4083)
test set	1949 (160)
B factor (Å^2)	
average	37.65
protein	24.87
RMSD bonds (Å)	0.014
RMSD angles (°)	1.21
Number of non-hydrogen atoms	
protein	2201
ligand	16
water	169
Ramachandran plot (%)	
most favored	98.44
additionally allowed	1.56
outliers	0.00

[a] $R_{merge} = \sum|I_i - I_m|/\sum I_i$, where I_i is the intensity of the measured reflection and I_m is the mean intensity of all symmetry related reflections.

[b] $R_{work} = \Sigma||F_{obs}| - |F_{calc}||/\Sigma|F_{obs}|$, where F_{obs} and F_{calc} are observed and calculated structure factors.

[c] $R_{free} = \Sigma_T||F_{obs}| - |F_{calc}||/\Sigma_T|F_{obs}|$, where T is a test data set of about 5% of the total reflections randomly chosen and set aside prior to refinement.

Numbers in parentheses represent the value for the highest resolution shell.